45th AIAA/ASME/SAE/ASEE Joint Propulsion Conference & Exhibit
2 - 5 August 2009, Denver, Colorado

AIAA 2009-5305

Energy Based Solutions of the Bidirectional Vortex with Multiple Mantles

Tony Saad* and Joseph Majdalani†
University of Tennessee Space Institute, Tullahoma, TN 37388

In a previous article, an energy optimization technique was used to derive multiple solutions for the bidirectional vortex. These were obtained for a single mantle describing a single flow reversal scenario. However, the existence of multiple mantles sustaining compound flow turns has been reported in previous work. The current study focuses on the application of the energy based optimization technique to the bidirectional vortex with multiple mantles. We follow a similar analysis and uncover two families of solutions, namely, Type I and Type II solutions with increasing or decreasing energy levels respectively. Both types approach the Type 0 reference solution either from below or above as the energy power index is increased. The solution with multiple mantles entertains a more versatile representation of the bidirectional vortex with allowance for additional physical mechanisms that the flowfield may sustain.

Nomenclature

a	= chamber radius
E_V	= Total volumetric kinetic energy
$\mathscr{E}$	= Kinetic Energy Density, $E_V/\kappa^2 l^3$
l	= normalized chamber length, $\bar{l}/a$
m	= number of mantles
$\bar{Q}_i$	= total inlet volumetric flowrate
Q_i	= normalized inlet volumetric flowrate, $\bar{Q}_i/(Ua^2)$
r, z	= normalized radial and axial coordinate, $\bar{r}/a$, $\bar{z}/a$
$\mathbf{u}$	= normalized velocity $(\bar{u}, \bar{v}, \bar{w})/U$
U	= mean inflow velocity $\bar{v}(a,\bar{l})$
η	= action variable, $m(2n+1)\pi r^2$
κ	= inflow parameter, $Q_i/2\pi l$
ρ	= density

Superscripts

$\bar{}$	= overbars denote dimensional variables
$^-$	= superscript denotes Type I solutions
$^+$	= superscript denotes Type II solutions

I. Introduction

IT may be argued that vortex dominated motions are among the most daunting and intriguing flows to model in fluid mechanics.[1-6] Over the past four decades, a substantial collection of research has come to light starting with the advent of boundary layer theory and aerodynamics whose prominent scientists, Prandtl and Von Karman have laid out essential foundations for analysis.[7-9] Yet, swirl dominated flows continue to present recurring challenges in view of their often counter intuitive behavior among fluid phenomena. The paradox of the irrotational vortex

*Doctoral Research Assistant, Mechanical, Aerospace and Biomedical Engineering Department. Member AIAA.
†H. H. Arnold Chair of Excellence in Advanced Propulsion, Mechanical, Aerospace and Biomedical Engineering Department. Senior Member AIAA. Fellow ASME.

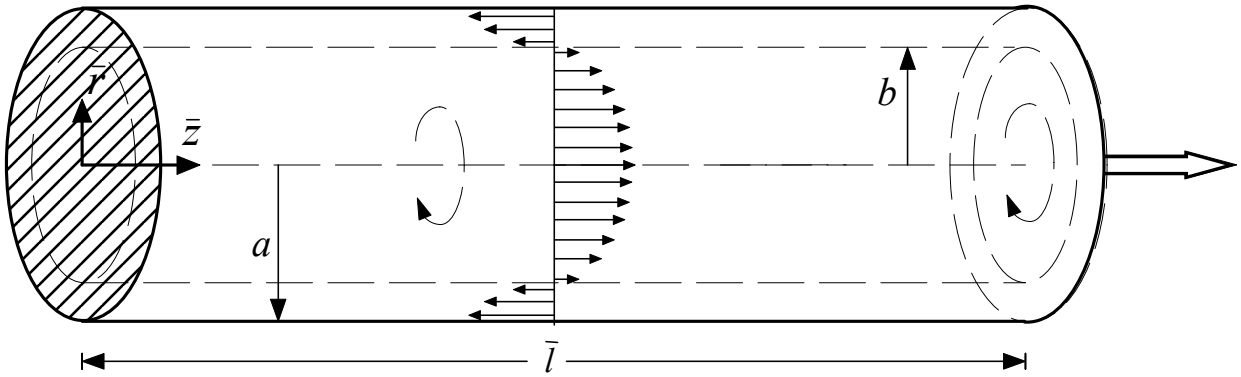

Figure 1. Confined bidirectional vortex in a right-cylindrical chamber.

constitutes one such example.[10] Sparked by recent interest in vortex-fired engine technology,[11-21] a substantial amount of research has focused on the modeling of vortex flows. From tornadoes[22] to cyclone separators,[23-25] theoretical models for these motions continue to unravel, albeit gradually, the key physical characteristics that are responsible for their behavior. Among the promising applications that come to mind, one may cite the bidirectional vortex-driven engine technology as an ideal platform for space propulsion. Its use is sparked by its superior cooling properties that may be connected to the two quasi-insulated regions that form in the chamber. In practice, the standard bidirectional vortex operates by injecting a fluid stream tangentially into a cylindrical chamber. Prompted by the rotating fluid layers, the fluid traverses the chamber in a corkscrew motion until it reaches the headwall. It then reverses direction and returns through the central region that discharges into a nozzle attachment plane. Note that fluid reversal does not only occur near the headwall. As recent studies have shown,[26-27] crossing into the inner core vortex takes place uniformly along the mantle. This interface separates the inner and outer vortex regions and will be further described below.

To the authors' knowledge, Vyas, Majdalani and Chiaverini[28] are among the first to provide a useful analytical model for the bidirectional vortex flowfield. Their analysis is further extended to describe solutions with multiple mantles,[29] viscous core corrections,[30] and sidewall boundary layers.[31-32] The search for general nonlinear solutions is also initiated by Majdalani and Rienstra.[26] In fact, two companion papers[33-34] introduce a class of new exact solutions for the bidirectional vortex in conical and cylindrical chambers.

A specific feature in the bidirectional vortex stands in its ability to sustain multiple passes and, hence, mantles. The mantle is defined as the surface inside the chamber where the axial velocity vanishes before changing its sign. The corresponding behavior is illustrated in Figs. 1 and 2a for a single mantle configuration where the mantle radius is denoted by b. However, as reported in previous studies,[29] multiple mantles can occur as a result of the flow undergoing a series of alternating reversals. Such behavior is depicted in Fig. 2b for a tri-mantle configuration.

In this paper, we implement an energy optimization methodology for the purpose of obtaining other approximations for the multidirectional vortex that are energy-based. A similar analysis was presented by the authors for the flow in porous cylinders and channels with arbitrary headwall injection.[35] It was also extended to the bidirectional vortex chamber with single mantle configuration.[36] Our study is prompted by the need to analytically approximate diverse flow configurations that may be sustained in thrust combustors. In these environments, several energy sources, such as acoustic excitation, energy release, compressibility and turbulence, come into play to alter the bulk gaseous motion. It is our hope to provide families of approximations that could mimic the ensuing flowfields. The solutions that we obtain will indeed exhibit steeper or smoother profiles depending on their energy signature. These will be bracketed and compared to the basic Type 0 solution presented by Vyas and Majdalani.[29]

II. Mathematical Model

The bidirectional vortex can be idealized as a cylinder of length $\bar{l}$ and radius a. Along the sidewall, the tangential velocity is assumed constant. A steady, inviscid, inert, and rotational flow is considered. These assumptions fall within the framework of a cold flow representation of the bidirectional vortex. The origin is taken at the head-end center and the solution domain is extended to the exit plane situated at $\bar{l}$. Near the exit plane, the flow is capable of undergoing several reversals that in turn will lead to the onset of a suitable number of mantles. The fluid is injected into the chamber at a given flowrate $\bar{Q}_i$. The injection port can be assumed to be an infinitely thin region in the inlet section. Furthermore, it is assumed that tangential injection will immediately trigger the

onset of axial and radial velocity distributions with no need for a flow development region.[37] The flow entering the chamber travels to the headwall using a helical path that reverses direction at the head-end. In the following sections, approximate solutions for the bidirectional vortex with multiple flow reversals will be developed.

A. Equations

We consider the inviscid flow equations

$$\frac{1}{\overline{r}}\frac{\partial\left(\overline{r}\overline{u}\right)}{\partial\overline{r}}+\frac{1}{\overline{r}}\frac{\partial\overline{v}}{\partial\theta}+\frac{\partial\overline{w}}{\partial\overline{z}}=0 \tag{1}$$

$$\overline{u}\frac{\partial\overline{u}}{\partial\overline{r}}+\frac{\overline{v}}{\overline{r}}\frac{\partial\overline{u}}{\partial\theta}+\overline{w}\frac{\partial\overline{u}}{\partial\overline{z}}-\frac{\overline{v}^2}{\overline{r}}=-\frac{1}{\rho}\frac{\partial\overline{p}}{\partial\overline{r}} \tag{2}$$

$$\overline{u}\frac{\partial\overline{v}}{\partial\overline{r}}+\frac{\overline{v}}{\overline{r}}\frac{\partial\overline{v}}{\partial\theta}+\overline{w}\frac{\partial\overline{v}}{\partial\overline{z}}+\frac{\overline{u}\,\overline{v}}{\overline{r}}=-\frac{1}{\rho\overline{r}}\frac{\partial\overline{p}}{\partial\theta} \tag{3}$$

$$\overline{u}\frac{\partial\overline{w}}{\partial\overline{r}}+\frac{\overline{v}}{\overline{r}}\frac{\partial\overline{w}}{\partial\theta}+\overline{w}\frac{\partial\overline{w}}{\partial\overline{z}}=-\frac{1}{\rho}\frac{\partial\overline{p}}{\partial\overline{z}} \tag{4}$$

where u, v, and w are the radial, tangential, and axial velocity components respectively. Reduction of the governing equations can be achieved through axisymmetry around the cylinder axis. This ensures the cancellation of all tangential derivatives. Another assumption can be made that renders the system of equations easily tractable. As an approximation based on previous studies,[27-28] one can relax the axial dependence of the tangential velocity. The case of axially dependent tangential velocity will be developed in later work. Implementation of these assumptions into the governing equations yields

$$\frac{1}{\overline{r}}\frac{\partial\left(\overline{r}\,\overline{u}\right)}{\partial\overline{r}}+\frac{\partial\overline{w}}{\partial\overline{z}}=0 \tag{5}$$

$$\overline{u}\frac{\partial\overline{u}}{\partial\overline{r}}+\overline{w}\frac{\partial\overline{u}}{\partial\overline{z}}-\frac{\overline{v}^2}{\overline{r}}=-\frac{1}{\rho}\frac{\partial\overline{p}}{\partial\overline{r}} \tag{6}$$

$$\overline{u}\frac{\partial\overline{v}}{\partial\overline{r}}+\overline{u}\frac{\overline{v}}{\overline{r}}=0 \tag{7}$$

$$\overline{u}\frac{\partial\overline{w}}{\partial\overline{r}}+\overline{w}\frac{\partial\overline{w}}{\partial\overline{z}}=-\frac{1}{\rho}\frac{\partial\overline{p}}{\partial\overline{z}} \tag{8}$$

B. Boundary Conditions

Five physical boundaries can be examined. These are

(a) tangential inflow at the sidewall;
(b) vanishing axial flow at the headwall;
(c) no cross-flow at the centerline;
(d) no radial inflow at the sidewall; and
(e) conservation of mass in the exit plane.

These can be translated into mathematical form as

$$\begin{cases}\overline{v}\left(a,\overline{l}\right)=U & \text{(tangential inflow)}\\ \overline{w}\left(\overline{r},0\right)=0 & \text{(vanishing axial flow at the headend)}\\ \overline{u}\left(0,\overline{z}\right)=0 & \text{(no cross-flow at the centerline)}\\ \overline{u}\left(a,\overline{z}\right)=0 & \text{(no radial inflow at the sidewall)}\\ \overline{Q}_o\left(\overline{l}\right)=\overline{Q}_i\left(\overline{l}\right) & \text{(matching inflow and outflow)}\end{cases} \tag{9}$$

C. Normalization

We use the following normalization for all recurring variables

$$z=\frac{\overline{z}}{a};\ r=\frac{\overline{r}}{a};\ \nabla=a\overline{\nabla};\ \beta_n=\frac{b_n}{a} \tag{10}$$

$$\mathbf{u}=\frac{\bar{\mathbf{u}}}{U};\ \ p=\frac{\bar{p}}{\rho U^2};\ \ \psi=\frac{\bar{\psi}}{a^2U_w};\ \ Q_i=\frac{\bar{Q}_i}{Ua^2}=\frac{A_i}{a^2};\ \ Q_o=\frac{\bar{Q}_o}{Ua^2} \tag{11}$$

Here, $U=\bar{v}(a,\bar{l})=\bar{Q}_i/A_i$ is the average injection velocity and b_j is radius of the j^{th} mantle. Upon normalization, the dimensionless boundary conditions become

$$\begin{cases} v(1,l)=1 & \text{(tangential inflow)} \\ w(r,0)=0 & \text{(vanishing axial flow at the headend} \\ u(0,z)=0 & \text{(no radial flow at the centerline)} \\ u(1,z)=0 & \text{(no radial inflow at the sidewall)} \\ \int_0^{2\pi}\int_0^1 \mathbf{u}(r,l)\cdot\hat{\mathbf{n}}\,r\,\mathrm{d}r\,\mathrm{d}\theta=0 & \text{(matching inflow and outflow)} \end{cases} \tag{12}$$

D. Decoupling of the Equations

The tangential component of the governing equations can be decoupled from the system using Eq. (7)

$$u\left(\frac{\partial v}{\partial r}+\frac{v}{r}\right)=0 \tag{13}$$

This yields the free vortex form of the tangential velocity v,

$$v=\frac{A}{r}=\frac{1}{r} \tag{14}$$

where the constant in Eq. (14) has been determined by application of the tangential flow requirement at the sidewall, Eq. (12)a. The singularity at the centerline is due to the inviscid nature of the flow.[27] This deficiency can be circumvented by the viscous core corrections that have been carried out by Batterson and Majdalani.[32]

E. Vorticity-Stream Function Decomposition

To make further headway, we make use of the vorticity transport and vorticity equations. For inviscid motion, these reduce to

$$\text{a) } \nabla\times(\mathbf{u}\times\boldsymbol{\Omega})=0\ ;\ \ \text{b) } \boldsymbol{\Omega}=\nabla\times\mathbf{u} \tag{15}$$

The Stokes stream function is then conveniently employed through

$$u=-\frac{1}{r}\frac{\partial\psi}{\partial z}\qquad\text{and}\qquad w=\frac{1}{r}\frac{\partial\psi}{\partial r} \tag{16}$$

We now substitute Eq. (16) into Eq. (15)a. This requires setting

$$\Omega=\Omega_\theta=rF(\psi) \tag{17}$$

We then select the simplest relation between Ω and ψ, namely,[38]

$$\Omega=C^2r\psi \tag{18}$$

By inserting Eq. (18) into the vorticity equation (Eq. (15)b), one eliminates Ω and uncovers the governing PDE for this problem. This is

$$\frac{\partial^2\psi}{\partial z^2}+\frac{\partial^2\psi}{\partial r^2}-\frac{1}{r}\frac{\partial\psi}{\partial r}+C^2r^2\psi=0 \tag{19}$$

with the particular set of constraints being:

$$\begin{cases} \text{(a)}\quad z=0:\quad w=0;\quad \partial\psi/\partial r=0; \\ \text{(b)}\quad r=0:\quad u=0;\quad \partial\psi/\partial z=0; \\ \text{(d)}\quad r=1:\quad u=0;\quad \partial\psi/\partial z=0; \\ \text{(d)}\quad \int_0^{2\pi}\int_0^1 \mathbf{u}(r,l)\cdot\hat{\mathbf{n}}\,r\,\mathrm{d}r\,\mathrm{d}\theta=0 \end{cases} \tag{20}$$

Note that Eq. (19) is a special form of the Bragg-Hawthorne equation[39] for axisymmetric Euler motions that may be solved by separation of variables; one finds the solution

$$\psi(r,z)=(\kappa_m\alpha z+\gamma)[A\cos(Cr^2)+B\sin(Cr^2)] \tag{21}$$

where

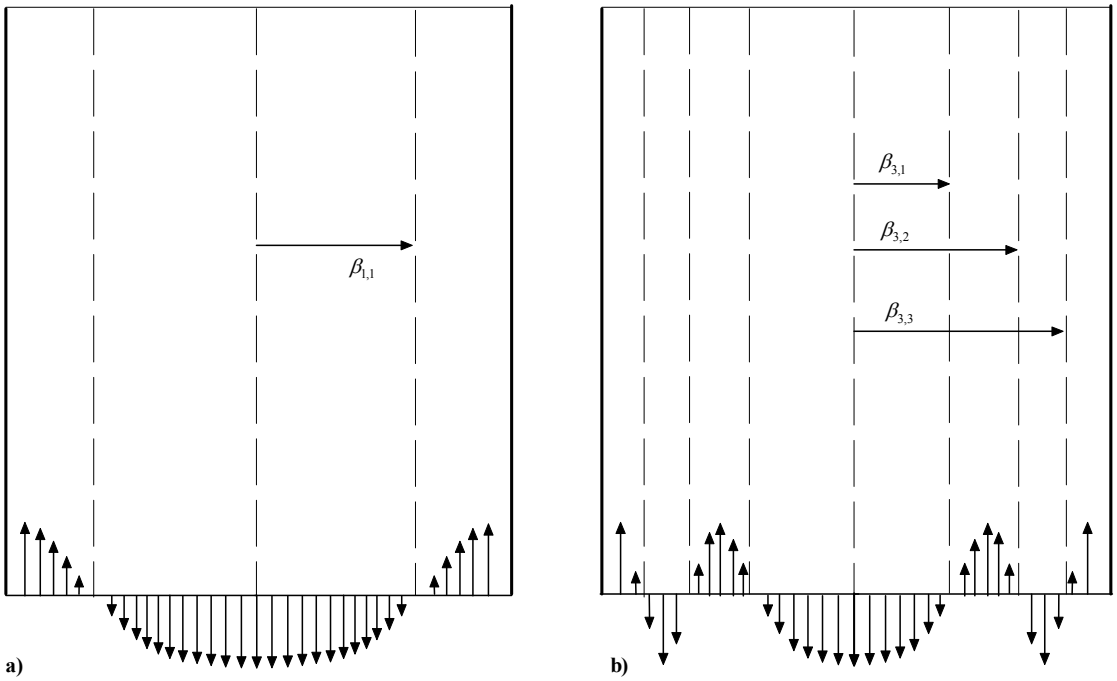

Figure 2. Multi-mantle configuration for the bidirectional vortex a) single mantle b) three mantles.

$$\kappa_m = \frac{\kappa}{m}\ ;\ \kappa = \frac{Q_i}{2\pi l} \tag{22}$$

is the inflow parameter and *m* denotes the number of mantles. The introduction of κ_m into Eq. (21) simplifies the solution process as it will be shown in subsequent sections.

III. Energy Triggered Solutions

A. Multi-mantle Eigenfunction Solution

The boundary conditions can now be used to determine the constants appearing in the general solution. Starting with Eq. (20)a

$$\frac{\partial \psi(r,0)}{\partial r} = \gamma[\tfrac{1}{2} C\, rA\cos(Cr^2) + \tfrac{1}{2} C\, rB\sin(Cr^2)] = 0 \tag{23}$$

or $\gamma = 0$. Next, application of Eq. (20)b yields

$$\frac{\partial \psi(0,z)}{\partial z} = \kappa_m \alpha A = 0 \tag{24}$$

since $\alpha \neq 0,$ then $A = 0$. Without loss of generality, one may set $B = 1$ and rewrite the present solution as

$$\psi(r,z) = \kappa_m \alpha z \sin(Cr^2) \tag{25}$$

Next, application of Eq. (20)c yields

$$\frac{\partial \psi(1,z)}{\partial z} = \kappa_m \alpha \sin(C) = 0 \tag{26}$$

or $\sin(C) = 0$. In order to derive energy based multiple solutions, one must choose an eigenfunction solution. Therefore, instead of the Type 0 solution given by $C = m\pi$,[27] we consider the general form of *C* as

$$C = C_k = m(k+1)\pi;\ k = \{0,1,2,...,\infty\} \in \mathbb{N} \tag{27}$$

where *m* is a multiplicity factor denoting the number of inner mantles for $m+1$ flow reversals. Summing over positive values of *k* enables us to recover an eigenfunction series solution. Subsequently, the energy optimization technique may be conveniently applied. One puts

$$\psi_k(r,z) = \kappa_m \alpha_k z \sin\left[m(k+1)\pi r^2\right] \quad \text{or} \quad \psi(r,z) = \sum_{k=0}^{\infty} \kappa_m \alpha_k z \sin\left[m(k+1)\pi r^2\right] \tag{28}$$

Finally, Eq. (20)d translates into a constraint equation for $\{\alpha_k\}$. From Eq. (20)d we obtain

$$2\pi\int_0^1 \mathbf{u}(r,l)\cdot\hat{\mathbf{n}}\, r\,\mathrm{d}r = 0 \tag{29}$$

The exit plane is divided into inflow and outflow rings demarcated by the mantles. This process is illustrated in Fig. 2. The first outflow port is located at $0 \le r \le \beta_{m,1}$ because the axial velocity vector at that surface points outwardly. The integral in Eq. (29) can be split into inflow and outflow regions, one can separate flow entering through the injecting surfaces whose net flowrate is Q_i. These are located between every other exit port shown in Fig. 2. At the outset, Eq. (29) is conveniently written as

$$2\pi\int_0^{\beta_{m,1}} \mathbf{u}(r,l)\cdot\hat{\mathbf{n}}\, r\,\mathrm{d}r + 2\pi\int_{\beta_{m,2}}^{\beta_{m,3}} \mathbf{u}(r,l)\cdot\hat{\mathbf{n}}\, r\,\mathrm{d}r + \ldots + 2\pi\int_{\beta_{m,2i}}^{\beta_{m,2i-1}} \mathbf{u}(r,l)\cdot\hat{\mathbf{n}}\, r\,\mathrm{d}r + \ldots = Q_i \tag{30}$$

or

$$\int_0^{\beta_{m,1}} \mathbf{u}(r,l)\cdot\hat{\mathbf{n}}\, r\,\mathrm{d}r + \sum_{i=1}^{(m-1)/2} \int_{\beta_{m,2i}}^{\beta_{m,2i+1}} \mathbf{u}(r,l)\cdot\hat{\mathbf{n}}\, r\,\mathrm{d}r + \delta_m \int_{\beta_{m,m}}^1 \mathbf{u}(r,l)\cdot\hat{\mathbf{n}}\, r\,\mathrm{d}r = \frac{Q_i}{2\pi} \tag{31}$$

where

$$\delta_m = \begin{cases} 1 & m \text{ even} \\ 0 & m \text{ odd} \end{cases} \tag{32}$$

Upon performing the integration, one can get rid of the constraint given by Eq. (32). We finally obtain the following convenient form

$$\sum_{i=1}^{m}\sum_{k=0}^{\infty} (-1)^{i+1} m^{-1}\alpha_k \sin\left[m(k+1)\pi\beta_{m,i}^2\right] = 1 \tag{33}$$

According to the formulation given by Eq. (31), and knowing that the innermost ring is always an outflow port, the outermost ring ($\beta_{m,m} \le r \le 1$) can either be an inflow or outflow port depending on the number of mantles. However, from a practical standpoint, the outmost ring is the contiguous surface to the injection manifolds and, in practice, can only be an injection port. Consequently, we only consider an odd number of mantles. This does not modify the character of the mathematical problem but rather narrows down the range of physically plausible solutions.

B. Mantle Locations

In order to simplify Eq. (33) it would be helpful to determine the values of $\beta_{m,j}$ that yield the theoretical locations of the mantles. Because the axial velocity vanishes[28] at a given mantle, we consider mantle *j* and write $w(\beta_{m,j}, z) = 0$. This translates into

$$\sum_{k=0}^{\infty} (k+1)\alpha_k \cos\left[m(k+1)\pi\beta_{m,j}^2\right] =$$

$$\alpha_0 \cos\left(m\pi\beta_{m,j}^2\right) + 2\alpha_1 \cos\left(2m\pi\beta_{m,j}^2\right) + 3\alpha_2 \cos\left(3m\pi\beta_{m,j}^2\right) + \ldots + (k+1)\alpha_k \cos\left[m(k+1)\pi\beta_{m,j}^2\right] = 0 \tag{34}$$

Each term in Eq. (34) has to vanish identically if Eq. (34) is to be satisfied. However, since $\{\alpha_k\}$ is nonzero then the cosine terms in Eq. (34) should be null for the same value of $\beta_{m,j}$. Since the first term in Eq. (34) corresponds to the Type 0 solution, it is always nonzero and hence can be used to extract the root:

$$\cos\left(m\pi\beta_{m,j}^2\right) = 0; \quad \text{or} \quad m\pi\beta_{m,j}^2 = \tfrac{1}{2}(2j+1)\pi \tag{35}$$

The mantles are therefore located at

$$\beta_{m,j} = \sqrt{\frac{2j-1}{2m}} \tag{36}$$

Equation (36) coincides with the multiple mantle locations derived in the Type 0 solution by Vyas and Majdalani.[29] Substitution of Eq. (36) into Eq. (34) reveals that the terms with odd indices do not vanish. Since all other coefficients are nonzero, and since the first term is always nonzero, the eigenfunction summation must to be carried out over all odd integers. We therefore put

$$C_k = m(k+1) = m(2n+1);\ n = \{0,1,2,\ldots,\infty\} \in \mathbb{N} \tag{37}$$

If, on the other hand, we had chosen to sum over even indices, it would have been impossible to obtain a single value of $\beta_{m,j}$ for which the cosine terms vanish. The only plausible solution in our case corresponds to the form given by Eqs. (37) and (35). Our superimposed solution becomes

$$\psi(r,z) = \sum_{n=0}^{\infty} \kappa_m \alpha_n z \sin\left[m(2n+1)\pi r^2\right] \tag{38}$$

With the mantle locations determined, we substitute Eq. (36) into Eq. (33) and set

$$\sum_{i=1}^{m}\sum_{n=0}^{\infty} (-1)^{i+1} m^{-1} \alpha_n \sin\left[\tfrac{1}{2}(2i-1)(2n+1)\pi\right] = 1 \tag{39}$$

This can be simplified into

$$\sum_{i=1}^{m}\sum_{n=0}^{\infty} (-1)^{i+1} m^{-1} \alpha_n \sin\left[\tfrac{1}{2}\left(4in+2i-2n-1\right)\pi\right] = \sum_{i=1}^{m}\sum_{n=0}^{\infty} (-1)^{i+1} m^{-1} \alpha_n \sin\left[i\pi - \tfrac{1}{2}(2n+1)\pi\right] = 1 \tag{40}$$

Finally, by considering odd and even values for *i*, Eq. (40) reduces to

$$m\sum_{n=0}^{\infty} (-1)^n m^{-1} \alpha_n = 1; \text{ or } \sum_{n=0}^{\infty} (-1)^n \alpha_n = 1 \tag{41}$$

C. Energy Optimization

Evidently, the choice of $\{\alpha_n\}$ is arbitrary provided that it satisfies the constraint given by Eq. (41). For the Type 0 solution, a simple model is given by $\alpha_0 = 1$ and $\alpha_n = 0 \ \forall \ n \geq 1$. Another family of solutions may be achieved through kinetic energy optimization. This model is prompted by the idea that a flow may choose the path of least or most energy expenditure. To examine this paradigm, we calculate the local kinetic energy at (r,z) for each eigensolution using

$$E_n(r,z) = \tfrac{1}{2}\boldsymbol{u}_n^2 = \tfrac{1}{2}(u_n^2 + w_n^2) \tag{42}$$

We also note that each eigenmode is an exact solution bearing the form

$$u_n = -\kappa_m \alpha_n r^{-1} \sin\eta; \qquad w_n = 2\pi\kappa(2n+1)\alpha_n z \cos\eta; \quad \eta \equiv m(2n+1)\pi r^2 \tag{43}$$

The tangential velocity, being decoupled from the system and the summation index, is excluded from the kinetic energy equation. This grants the tangential velocity a quasi universal character among the energy-dependent solutions because its contribution to the kinetic energy remains the same irrespective of the energy level.

Our next step is to define the cumulative local energy. To do this, we assume a system of eigensolutions, each with an individual kinetic energy, given by Eq. (42). Subsequently, the local cumulative energy may be written as

$$E_L = \sum_{n=0}^{\infty} E_n(r,z) = \tfrac{1}{2}\sum_{n=0}^{\infty}\left[\kappa_m^2\alpha_n^2 r^{-2}\sin^2\eta + 4\pi^2\kappa^2(2n+1)^2\alpha_n^2 z^2\cos^2\eta\right] \tag{44}$$

Finally, one can evaluate the total kinetic energy in the chamber volume V by integrating the local kinetic energy over the chamber length and cross-section,

$$E_V = \int_0^{2\pi}\int_0^{l}\int_0^{1} E_L \, r\,\mathrm{d}r\,\mathrm{d}z\,\mathrm{d}\theta = \pi\sum_{n=0}^{\infty}\int_0^{l}\int_0^{1}\left[\kappa_m^2\alpha_n^2 r^{-2}\sin^2\eta + 4\pi^2\kappa^2(2n+1)^2\alpha_n^2 z^2\cos^2\eta\right] r\,\mathrm{d}r\,\mathrm{d}z \tag{45}$$

Upon integration and simplification, we obtain

$$E_V = \tfrac{1}{12}\pi^3\kappa^2 l^3 \sum_{n=0}^{\infty}\alpha_n^2 a_n + l^{-2}\pi^{-2}\alpha_n^2 b_n \tag{46}$$

where

$$a_n = 4(2n+1)^2; \quad b_n = 3m^{-2}\,\mathrm{Cin}\left[2m(2n+1)\pi\right] \tag{47}$$

Here $\mathrm{Cin}(x) = \int_0^x (1-\cos t)t^{-1}\,\mathrm{d}t$ is the entire cosine integral. We now seek to find an extremum of the total kinetic energy subject to the fundamental constraint

$$\sum_{n=0}^{\infty}(-1)^n\alpha_n = 1 \tag{48}$$

The method of Lagrangian multipliers may be conveniently utilized by first defining the constrained energy function

$$g = E_V + \lambda\left[\sum_{n=0}^{\infty}(-1)^n\alpha_n - 1\right] \tag{49}$$

By imposing $\nabla g(\alpha_0,\alpha_1,\alpha_2,...,\lambda) = 0$, one can find the extremum of Eq. (49). In shorthand notation, we write

$$\nabla g(\alpha_n,\lambda) = 0 \quad n = \{0,1,2...,\infty\} \tag{50}$$

Subsequently, Eq. (49) may be differentiated with respect to each of its variables to obtain

$$\frac{\partial g}{\partial \alpha_n} = \tfrac{1}{6}\pi^3\kappa^2 l^3 \alpha_n \left(a_n + \pi^{-2} l^{-2} b_n\right) + (-1)^n \lambda = 0; \quad n = \{0,1,2...,\infty\} \tag{51}$$

$$\frac{\partial g}{\partial \lambda} = \sum_{n=0}^{\infty} (-1)^n \alpha_n - 1 = 0 \tag{52}$$

Equation (51) can be solved for $\{\alpha_n\}$ in terms of λ such that

$$\alpha_n = -\frac{6\pi^{-3}\kappa^{-2} l^{-3} (-1)^n \lambda}{a_n + \pi^{-2} b_n l^{-2}} \tag{53}$$

This can be suitably substituted into Eq. (52) to retrieve

$$\lambda = -\frac{\pi^3 \kappa^2 l^3}{6\sum_{n=0}^{\infty} (a_n + \pi^{-2} l^{-2} b_n)^{-1}} \tag{54}$$

Finally, the general solution for $\{\alpha_n\}$ is obtained by substituting λ into Eq. (53)

$$\alpha_n = \frac{(-1)^n}{\left(a_n + \pi^{-2} L^{-2} b_n\right) \sum_{i=0}^{\infty} \left(a_i + \pi^{-2} l^{-2} b_i\right)^{-1}} \tag{55}$$

The total energy given by Eq. (46) is now fully determined. A close inspection of this expression reveals that one can segregate $\kappa^2 l^3$ from the remaining terms to obtain a more convenient form. It is then useful to introduce a suitable form of energy density such as $\mathscr{E} = E_V / (\kappa^2 l^3)$. Then, by plotting $\mathscr{E}$ versus l in Fig. 3, one is able to assess the energy requirements associated with the multi-mantle bidirectional vortex. One also finds that as the length of the chamber is increased at fixed radius, $\mathscr{E}$ approaches a constant asymptotic value of $\mathscr{E}_\infty^- = 8\pi/3 \simeq 8.3776$. Interestingly, as the number of mantles increases, the kinetic energy density approaches the same asymptotic value of $8\pi/3$. This explains the flattening of the curves in Fig. 3 as *m* is increased. Our physical interpretation is as follows: when the number of mantles is increased, the axial flow becomes nearly uniform with alternating inflow and outflow velocities at a given cross-section. The separation between the inflow and outflow ports becomes infinitesimally small for large *m*. When the kinetic energy is computed by squaring the velocities, the configuration becomes nearly uniform, approaching a top hat profile. The radial velocity distribution, being inversely proportional to *m*, diminishes to accommodate the reduced flowrates crossing each mantle. Hence, once the radial velocity is squared, its contribution to the kinetic energy becomes negligible for large *m*. This reduction in the radial velocity explains the reason for the marked decrease in kinetic energy with successive increases in the number of mantles.

D. Critical Length

With the kinetic energy reaching an asymptotic value as the chamber length is increased, we define a critical aspect ratio l_{cr} beyond which the kinetic energy will vary by less than 1% from its final asymptotic value $\mathscr{E}_\infty^-$, i.e. $\mathscr{E} - \mathscr{E}_\infty^- \le 0.01\,\mathscr{E}_\infty^-$. For a chamber with $l \ge l_{cr}$, one may safely assume that $l \to \infty$ in evaluating Eq. (55), thereby achieving a substantial reduction in complexity. The critical length for a single mantle configuration can be calculated to be 3.95125. This critical length is inversely proportional to the number of mantles as can be implied from Fig. 3. Illustrative values are 1.58136 and 1.01567 for three and five mantles respectively. These relatively small values for the critical length hold practical implications for design considerations as the models presented herein can be further reduced by letting $l \to \infty$ without appreciable loss in precision.

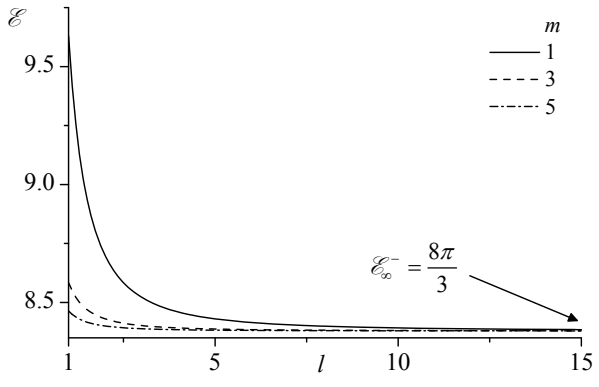

Figure 3. Kinetic energy variation vs. chamber length *l* for 1, 3, and 5 mantles.

E. Critical Number of Mantles

With a fixed length and radius, the kinetic energy reaches the same asymptotic limit as the number of

mantles m is increased. One can therefore define a critical number of mantles m_{cr} beyond which the kinetic energy will vary by less than 1% of its final asymptotic value. These are calculated to be 6 for l =1 and 3 for l =2.

F. Long Chambers

To corroborate our previous discussion, a simple test case may be used for a vortex chamber with an aspect ratio that exceeds l_{cr}. Letting $l \to \infty$, Eq. (55) reduces to

$$\alpha_n = (-1)^n \left(a_n \sum_{i=0}^{\infty} a_i^{-1} \right)^{-1} = \frac{8(-1)^n}{\pi^2 (2n+1)^2} \tag{56}$$

This relation identically satisfies the fundamental constraint expressed through Eq. (48).

G. Least Kinetic Energy Solution

The Lagrangian optimization technique enabled us to identify the problem's extremum with no indication of whether the solution corresponds to a minimum or a maximum. This does not pose a problem because substitution of Eq. (56) into Eq. (46) enables us to evaluate the nature of the extremum. Then, by comparing its value to the Type 0 solution, we are able to identify whether we have come across a minimum or a maximum. As we follow this process, we find that the solution corresponds to the flowfield with least kinetic energy in comparison with the Type 0 solution.

When $l \to \infty$ the streamfunction carrying the least kinetic energy that emerges from Eq. (28) may be expressed as

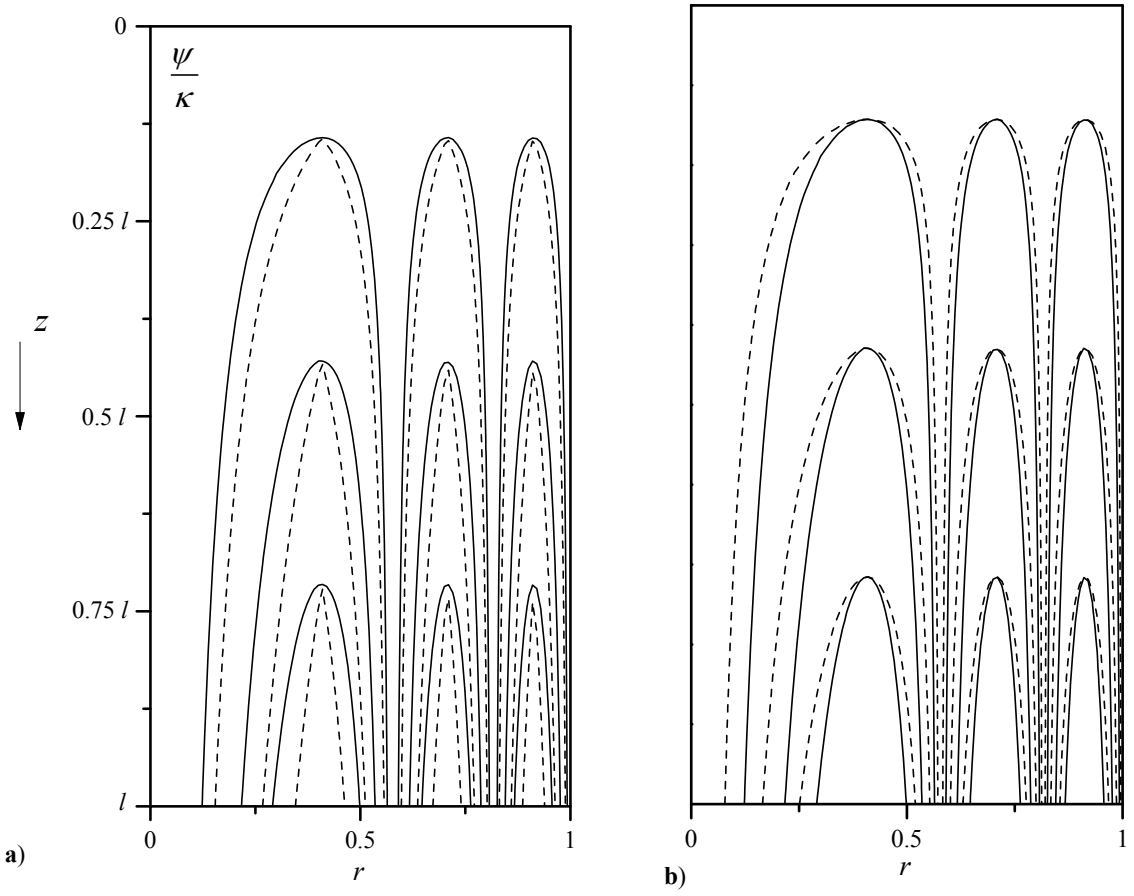

Figure 4. Flow streamlines for a tri-mantle configuration using either (a) Type I solutions (left) with increasing energy levels or (b) Type II solutions (right) with decreasing energy levels. The solid lines refer to the Type 0 solution.

$$\psi(r,z) = \frac{8\kappa}{\pi^2 m} z \sum_{n=0}^{\infty} \frac{(-1)^n}{(2n+1)^2} \sin\left[m(2n+1)\pi r^2 \right] \tag{57}$$

This is illustrated in Fig. 4a and compared to the Type 0 streamfunction. Using broken lines, the energy-minimized solution is shown to exhibit steeper curvatures. Such curvatures are typically associated with turbulent or compressible flow motions.[40] The corresponding radial and axial velocities may be derived from Eq. (57). These are posted in Table 1 below.

IV. Generalization

The solution obtained herein describes the flowfield carrying the minimum kinetic energy. Nevertheless, when $l \to \infty$, a close inspection of Eq. (56) reveals it comprises the key parameters that control the energy level for a given flowfield. Since $\{\alpha_n\}$ is left arbitrary, a more general family of solutions bearing different kinetic energies can be identified by altering the form of $\{\alpha_n\}$. It would also be informative to rank the Type 0 solution given by Vyas and Majdalani[27] according to its energy content within the set of possible solutions. To this end, we consider long chambers and make use of Eq. (56) as a guide.

A. Type I Solutions with Increasing Energy Levels

The first alternative formulation for $\{\alpha_n\}$ may be introduced by first noting that

$$\alpha_n = \frac{8(-1)^n}{\pi^2 (2n+1)^2} \sim \frac{(-1)^n A_2}{(2n+1)^2} \tag{58}$$

where $A_2 = 8/\pi^2$ can be deduced from the constraint given by Eq. (48). Its subscript is connected with the power of $(2n+1)$ in the denominator. To generalize, one defines the generic Type I form

$$\alpha_n^-(q) = \frac{(-1)^n A_q}{(2n+1)^q}; \quad q \geq 2 \tag{59}$$

where $q = 2$ reproduces the state of least energy expenditure. This relation will be made to satisfy Eq. (48) when

$$\sum_{n=0}^{\infty} (-1)^n \frac{(-1)^n A_q}{(2n+1)^q} = 1 \qquad \text{or} \qquad A_q = \frac{1}{\sum_{n=0}^{\infty} (2n+1)^{-q}} = \frac{1}{\zeta(q)(1-2^{-q})}; \quad \zeta(q) = \sum_{k=1}^{\infty} k^{-q} \tag{60}$$

where ζ is Riemann's zeta function and the exponent q is the *kinetic energy power index*. Note that the $q \geq 2$ condition is needed to ensure series convergence down to the vorticity. Backward substitution enables us to collect the proper form of $\{\alpha_n\}$, namely,

$$\alpha_n^-(q) = (-1)^n (2n+1)^{-q} \left[\sum_{k=0}^{\infty} (2k+1)^{-q} \right]^{-1} = \frac{(-1)^n (2n+1)^{-q}}{\zeta(q)(1-2^{-q})}; \quad q \geq 2 \qquad \text{(Type I)} \tag{61}$$

The 'minus' sign in the superscript denotes energies that are lower than the Type 0 solution. With the form given by Eq. (61), one can plot the variation of the total kinetic energy versus the kinetic energy power index q. This plot is

Table 1. Summary of solutions with least or most kinetic energies as well as the reference solution

Quantity	Type I	Type 0	Type II
ψ	$\frac{8\kappa}{\pi^2 m} z \sum_{n=0}^{\infty} \frac{(-1)^n}{(2n+1)^2} \sin\eta$	$\kappa m^{-1} z \sin(m\pi r^2)$	$\frac{\kappa}{\mathscr{C} m} z \sum_{n=0}^{\infty} \frac{1}{(2n+1)^2} \sin\eta$
u	$-\frac{8\kappa}{\pi^2 mr} \sum_{n=0}^{\infty} \frac{(-1)^n}{(2n+1)^2} \sin\eta$	$-\kappa m^{-1} r^{-1} \sin(m\pi r^2)$	$-\frac{\kappa}{\mathscr{C} mr} \sum_{n=0}^{\infty} \frac{1}{(2n+1)^2} \sin\eta$
w	$\frac{16\kappa}{\pi} z \sum_{n=0}^{\infty} \frac{(-1)^n}{(2n+1)} \cos\eta$	$2\pi\kappa z \cos(m\pi r^2)$	$\frac{2\pi\kappa}{\mathscr{C}} z \sum_{n=0}^{\infty} \frac{1}{(2n+1)} \cos\eta$
ω_θ	0	$4\pi^2 m\kappa r z \sin(m\pi r^2)$	$\frac{2\pi^2 m\kappa}{\mathscr{C}} rz \csc(\pi r^2)$

shown in Fig. 4a for several aspect ratios and mantle configurations. Interestingly, as $q \to \infty$, the Type 0 solution is strictly recovered. In fact, using Eq. (61), it can be rigorously demonstrated that

$$\lim_{q\to\infty} \alpha_n^- (q) = \begin{cases} 1; & n = 0 \\ 0; & \text{otherwise} \end{cases} \tag{62}$$

This result identically reproduces the Type 0 solution. All of the Type I formulations that can be precipitated from Eq. (61) possess kinetic energies that are lower than the Type 0. They can be bracketed between Eq. (57) and $\psi(r,z) = \kappa_m z \sin(m\pi r^2)$.

B. Type II Solutions with Decreasing Energy Levels

If the $(-1)^n$ multiplier in Eq. (59) is excluded, a new family of solutions with energies exceeding that the Type 0 emerge. One may set

$$\alpha_n^+ (q) = \frac{B_q}{(2n+1)^q}; \quad q \geq 2 \tag{63}$$

Again, the 'plus' sign in the superscript denotes higher energies. The remaining steps follow similar lines as before. Substitution into Eq. (48) unravels

$$\sum_{n=0}^{\infty} (-1)^n \frac{B_q}{(2n+1)^q} = 1 \quad \text{or} \quad B_q = \frac{1}{\sum_{n=0}^{\infty} (-1)^n (2n+1)^{-q}} = \frac{4^q}{\zeta(q,\frac{1}{4}) - \zeta(q,\frac{3}{4})} \tag{64}$$

where $\zeta(q,a) = \sum_{k=0}^{\infty} (k+a)^{-q}$ is the generalized Riemann zeta function. Equation (64) enables us to recover

$$\alpha_n^+ (q) = (2n+1)^{-q} \left[\sum_{k=0}^{\infty} (-1)^k (2k+1)^{-q} \right]^{-1} = \frac{4^q (2n+1)^{-q}}{\zeta(q,\frac{1}{4}) - \zeta(q,\frac{3}{4})} \quad \text{(Type II)} \tag{65}$$

All Type II solutions emerging from Eq. (65) dispose of higher kinetic energies than the Type 0 solution. The variation of the kinetic energy with respect to q is illustrated in Fig. 4b for several aspect ratios and mantle configurations. According to this form of $\{\alpha_n^+\}$, the Type 0 model proposed by Vyas and Majdalani[27] is recoverable asymptotically by taking the limit as $q \to \infty$. This expected result confirms that the Type 0 solution constitutes an equilibrium state to which other energy formulations duly converge.

For the solution with most kinetic energy (Type II, $q = 2$), Catalan's constant emerges in Eq. (65) in the form

$$\mathscr{C} = \sum_{k=0}^{\infty} (-1)^k (2n+1)^{-2} \simeq 0.915966 \tag{66}$$

The streamlines corresponding to this case, i.e. most kinetic energy, are plotted in Fig. 4b. The Type II approximation is seen to overshoot the Type 0 streamline curvature. Note that up to this point, the large aspect ratio limit has been used solely in the computation of the injection sequence, not in the kinetic energy expression.

C. Velocity

Differentiation of the streamfunction yields the radial and axial velocities

$$u = -\kappa_m r^{-1} \sum_{n=0}^{\infty} \alpha_n \sin\eta \; ; \quad w = 2\kappa\pi z \sum_{n=0}^{\infty} (2n+1)\, \alpha_n \cos\eta \tag{67}$$

These expressions are evaluated for the Type 0, I, and II solutions ($q = 2$) and posted in Table 1.

D. Vorticity

The vorticity is obtained using

$$\Omega_\theta = \frac{\partial u}{\partial z} - \frac{\partial w}{\partial r} = 4\pi^2 m\kappa r z \sum_{n=0}^{\infty} (2n+1)^2\, \alpha_n \sin\eta \tag{68}$$

This is evaluated for the least and most kinetic energy formulations ($q = 2$) as well as the reference solution. These are posted in Table 1.

E. Asymptotic Analysis of the Kinetic Energy Density

The kinetic energy density limits can be computed by letting $l \to \infty$. This is written as

$$\mathscr{E}_\infty = \tfrac{1}{3}\pi^3 \sum_{n=0}^{\infty} (2n+1)^2\, \alpha_n^2 = \mathscr{E}_\infty^\infty \sum_{n=0}^{\infty} (2n+1)^2\, \alpha_n^2 \tag{69}$$

where $\mathscr{E}_\infty^\infty \equiv \pi^3/3 \simeq 10.335$ denotes the asymptotic limit of the kinetic energy of the Type 0 solution ($L \to \infty$ and $q \to \infty$). By using the proper form of $\{\alpha_n\}$, one can evaluate the Type I and Type II limits. For the Type I, use of Eq. (61) yields

$$\mathscr{E}_\infty^-(q) = \mathscr{E}_\infty^\infty \left[\sum_{k=0}^{\infty} (2k+1)^{-q}\right]^{-2} \sum_{n=0}^{\infty} (2n+1)^{2-2q} = \mathscr{E}_\infty^\infty \frac{4^q - 4}{(2^q-1)^2} \frac{\zeta(2q-2)}{[\zeta(q)]^2} \tag{70}$$

In like manner, for the Type II solutions, Eq. (65) leads to

$$\mathscr{E}_\infty^+(q) = \mathscr{E}_\infty^\infty \left[\sum_{k=0}^{\infty} (-1)^k (2k+1)^{-q}\right]^{-2} \sum_{n=0}^{\infty} (2n+1)^{2-2q} = \mathscr{E}_\infty^\infty \frac{4^q(4^q-4)\zeta(2q-2)}{[\zeta(q,\tfrac{1}{4}) - \zeta(q,\tfrac{3}{4})]^2} \tag{71}$$

Specific values of these limits are calculated to be $\mathscr{E}_\infty^-(2) = 8\pi/3 \simeq 8.377$, $\mathscr{E}_\infty^-(4) = 16\pi/5 \simeq 10.053$, and $\mathscr{E}_\infty^-(6) = 620\pi/189 \simeq 10.305$ for the Type I, and $\mathscr{E}_\infty^+(2) \simeq 15.197$, $\mathscr{E}_\infty^+(4) \simeq 10.583$, and $\mathscr{E}_\infty^+(6) \simeq 10.362$ for the Type II.

It is interesting to note that both types approach $\mathscr{E}_\infty^\infty$ either from below or above. This is shown in Fig. 5 where the Type 0 solution is seen to bisect the range of possible energy excursions that are sustained by both Type I and II solutions. In practice, all solutions with $q \geq 5$ will be indiscernible from the Type 0 solution as their energies will differ by less than 1%. For the Type I solutions, the most distinct formulations correspond to $q = 2$, 3, and 4 with energies that are 81.06, 91.7, and 97.26% of the Type 0 solution. Similarly, for the Type II solutions, these are 47.04, 8.08, and 2.40% higher. Note that the asymptotic limit of 10.335 corresponding to the Type 0 solution is practically reached by both Type I and Type II solutions with differences of less than 0.287 and 0.265% at $q = 6$. This behavior is illustrated in Fig. 6. Given the maximum range at $q = 2$, the total allowable excursion in energy that the mean flow can undergo may be readily estimated at $\left[\mathscr{E}_\infty^+(2) - \mathscr{E}_\infty^-(2)\right]/\mathscr{E}_\infty^\infty = 66.0\%$, an appreciable portion of the available energy.

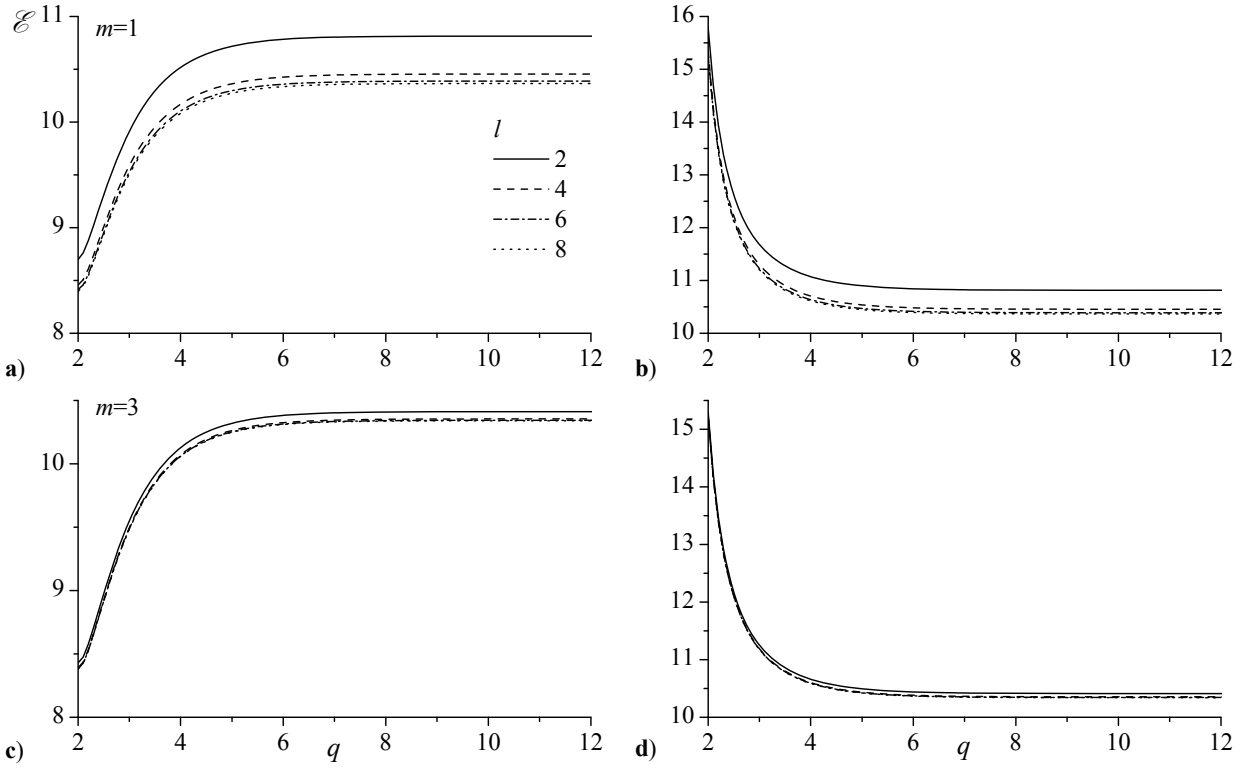

Figure 5. Total kinetic energy density in a vortex chamber for either (a,c) Type I solutions (left) with increasing energy levels or (b,d) Type II solutions (right) with decreasing energy levels. Results are for *l* = 2, 4, 6, and 8 with *m* = 1, 3.

V. Conclusions

In this study, we have applied the Lagrangian energy optimization technique to obtain two sets of alternate approximations for the bidirectional vortex with multiple flow reversals. The bidirectional vortex has been gaining interest in the propulsion community as an efficient flow mechanism to promote thrust and engine performance, by leveraging its lightweight usage, simplicity, and superior self-cooling properties. The new solutions that we have uncovered are accompanied by lower or higher kinetic energies that vary up to 66% of their mean value. The mean refers to the Type 0 inviscid model derived by Vyas and Majdalani.[27] The energy optimization technique enables us to pinpoint the flow with the least kinetic energy. The key parameter being the main injection sequence is identified to be $\alpha_n^- \sim (-1)^n (2n+1)^{-2}$ in this case. A generalization is subsequently presented to the extent that similar Type I solutions are uncovered in ascending order. This is achieved by introducing $\alpha_n^- \sim (-1)^n (2n+1)^{-q};\ q > 2$ where q is the energy power index. Interestingly, the Type 0 model is recovered asymptotically in the limit as $q \to \infty$. In practice, however, most solutions become indiscernible from the Type 0 solution for $q \geq 5$. Those obtained with $q = 2$, 3, and 4 exhibit energies that are 18.9, 8.28 and 2.73% lower than their remaining counterparts. When the same analysis is repeated using a modified form of the sequence $\alpha_n^+ \sim (2n+1)^{-q};\ q \geq 2$, a second family of solutions is identified and coined Type II. Its constituents dispose of higher energies than the Type 0 which is also recovered asymptotically when $q \to \infty$. Their most notable profiles correspond to $q = 2$, 3, and 4 with energies that are 47.0, 8.08, and 2.40% higher than the Type 0 solution. In the absence of experimental validation, our formulations remain academic although they increase our repertoire of engineering approximations and open up new avenues for representing profiles of varying steepness that may be encountered in the laboratory.

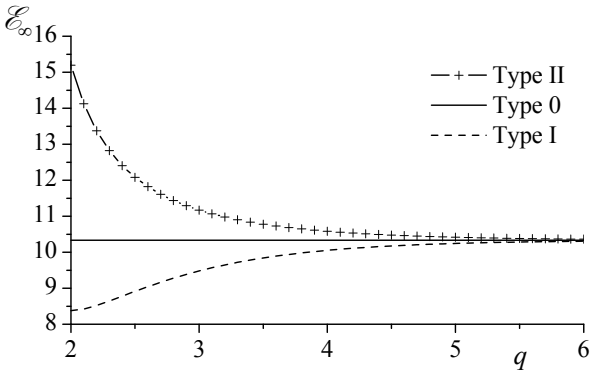

Figure 6. Asymptotic limits of the kinetic energy density for large *l* showing rapid convergence of both Type I and Type II solutions to the Type 0 value of 10.335.

Acknowledgments

This project was funded by the National Science Foundation through grant No. CMMI-0353518, Dr Eduardo A. Misawa, Program Director.

References

[1]Leibovich, S., and Kribus, A., "Large-Amplitude Wavetrains and Solitary Waves in Vortices," *Journal of Fluid Mechanics,* Vol. 216, No. 1, 1990, pp. 459-504.

[2]Escudier, M. P., "Vortex Breakdown - Observations and Explanations," *Progress in Aerospace Sciences,* Vol. 25, No. 2, 1988, pp. 189-229.

[3]Leibovich, S., "Vortex Stability and Breakdown: Survey and Extension," *AIAA Journal,* Vol. 22, No. 9, 1984, pp. 1192-1206.

[4]Escudier, M. P., and Zehnder, N., "Vortex-Flow Regimes," *Journal of Fluid Mechanics,* Vol. 115, No. 1, 1982, pp. 105-121.

[5]Leibovich, S., "The Structure of Vortex Breakdown," *Annual Review of Fluid Mechanics,* Vol. 10, 1978, pp. 221-246.

[6]Cortes, C., and Gil, A., "Modeling the Gas and Particle Flow inside Cyclone Separators," *Progress in Energy and Combustion Science,* Vol. in Press, 2007.

[7]von Kármán, T., and Burgers, J. M., "General Aerodynamic Theory – Perfect Fluids," *Aerodynamic Theory*, Vol. II, edited by W. F. Durand, Dover Publications, New York, 1963, pp. 216-221.

[8]von Kármán, T., and Burgers, J. M., "General Aerodynamic Theory – Perfect Fluids," *Aerodynamic Theory*, Vol. II, edited by W. F. Durand, Julius Springer-Verlag, Berlin, 1934, pp. 216-221.

[9]Prandtl, L., "Tragflügeltheorie I. Mitteilungen," *Gesammelte Abhandlungen,* Vol. 1, 1918, pp. 332-345.

[10]White, F. M., *Viscous Fluid Flow*, McGraw-Hill, New York, 1991.

[11]Rom, C. J., Anderson, M. H., and Chiaverini, M. J., "Cold Flow Analysis of a Vortex Chamber Engine for Gelled Propellant Combustor Applications," AIAA Paper 2004-3359, July 2004.
[12]Chiaverini, M. J., Malecki, M. J., Sauer, J. A., Knuth, W. H., and Majdalani, J., "Vortex Thrust Chamber Testing and Analysis for O2-H2 Propulsion Applications," AIAA Paper 2003-4473, July 2003.
[13]Anderson, M. H., Valenzuela, R., Rom, C. J., Bonazza, R., and Chiaverini, M. J., "Vortex Chamber Flow Field Characterization for Gelled Propellant Combustor Applications," AIAA Paper 2003-4474, July 2003.
[14]Sauer, J. A., Malecki, M. M., Knuth, W. H., Chiaverini, M. J., and Hall, C. D., "Development of a LOX/RP-1 Vortex Combustion Cold-Wall Thrust Chamber Assembly," AAIA Paper 2002-4144, July 2002.
[15]Knuth, W. H., Chiaverini, M. J., Sauer, J. A., and Gramer, D. J., "Solid-Fuel Regression Rate Behavior of Vortex Hybrid Rocket Engines," *Journal of Propulsion and Power,* Vol. 18, No. 3, 2002, pp. 600-609.
[16]Chiaverini, M. J., Malecki, M. M., Sauer, J. A., Knuth, W. H., and Hall, C. D., "Testing and Evaluation of Vortex Combustion Chamber for Liquid Rocket Engines," JANNAF April 2002.
[17]Chiaverini, M. J., Malecki, M. J., Sauer, J. A., and Knuth, W. H., "Vortex Combustion Chamber Development for Future Liquid Rocket Engine Applications," AIAA Paper 2002-2149, July 2002.
[18]Chiaverini, M. J., Sauer, J. A., and Knuth, W. K., "Final Report on Vortex Combustion Combined Cycle Engine- a Phase I SBIR Project," Orbital Technological Corporation, Air Force Contract No. F04611-99-C-0063 Rept. OTC-GS082-FR-99-1, March 1999.
[19]Knuth, W. H., Chiaverini, M. J., Gramer, D. J., and Sauer, J. A., "Experimental Investigation of a Vortex-Driven High-Regression Rate Hybrid Rocket Engine," AIAA Paper 98-3348, July 1998.
[20]Knuth, W. H., Bemowski, P. A., Gramer, D. J., Majdalani, J., and Rothbauer, W. J., "Gas-Fed, Vortex Injection Hybrid Rocket Engine," NASA Marshall Space Flight Center, SBIR Phase I Final Technical Rept. NASA/MSFC Contract NAS8-40679, Huntsville, AL, August 1996.
[21]Matveev, I., Matveeva, S., and Serbin, S., "Design and Preliminary Test Results of the Plasma Assisted Tornado Combustor," AIAA Paper 2007-5628, July 2007.
[22]Penner, S. S., "Elementary Considerations of the Fluid Mechanics of Tornadoes and Hurricanes," *Acta Astronautica,* Vol. 17, 1972, pp. 351-362.
[23]Reydon, R. F., and Gauvin, W. H., "Theoretical and Experimental Studies of Confined Vortex Flow," *The Canadian Journal of Chemical Engineering,* Vol. 59, 1981, pp. 14-23.
[24]Smith, J. L., "An Analysis of the Vortex Flow in the Cyclone Separator," *Journal of Basic Engineering-Transactions of the ASME*, 1962, pp. 609-618.
[25]Smith, J. L., "An Experimental Study of the Vortex in the Cyclone Separator," *Journal of Basic Engineering-Transactions of the ASME*, 1962, pp. 602-608.
[26]Majdalani, J., and Rienstra, S. W., "On the Bidirectional Vortex and Other Similarity Solutions in Spherical Coordinates," *Journal of Applied Mathematics and Physics (ZAMP),* Vol. 58, No. 2, 2007, pp. 289-308.
[27]Vyas, A. B., and Majdalani, J., "Exact Solution of the Bidirectional Vortex," *AIAA Journal,* Vol. 44, No. 10, 2006, pp. 2208-2216.
[28]Vyas, A. B., Majdalani, J., and Chiaverini, M. J., "The Bidirectional Vortex. Part 1: An Exact Inviscid Solution," AIAA Paper 2003-5052, July 2003.
[29]Vyas, A. B., Majdalani, J., and Chiaverini, M. J., "The Bidirectional Vortex. Part 3: Multiple Solutions," AIAA Paper 2003-5054, July 2003.
[30]Vyas, A. B., Majdalani, J., and Chiaverini, M. J., "The Bidirectional Vortex. Part 2: Viscous Core Corrections," AIAA Paper 2003-5053, July 2003.
[31]Vyas, A. B., and Majdalani, J., "Characterization of the Tangential Boundary Layers in the Bidirectional Vortex Thrust Chamber," AIAA Paper 2006-4888, July 2006.
[32]Batterson, J. W., and Majdalani, J., "On the Boundary Layers of the Bidirectional Vortex," AIAA Paper 2007-4123 June 2007.
[33]Majdalani, J., "Exact Eulerian Solutions of the Cylindrical Bidirectional Vortex," AIAA Paper 2009-5307, August 2009.
[34]Barber, T. A., and Majdalani, J., "Exact Eulerian Solution of the Conical Bidirectional Vortex," AIAA Paper 2009-5306, August 2009.
[35]Majdalani, J., and Saad, T., "Energy Steepened States of the Taylor-Culick Profile," AIAA Paper 2007-5797, July 2007.
[36]Saad, T., and Majdalani, J., "Energy Based Solutions of the Bidirectional Vortex," AIAA Paper 2008-4832, July 2008.

[37]Bloor, M. I. G., and Ingham, D. B., "The Flow in Industrial Cyclones," *Journal of Fluid Mechanics,* Vol. 178, No. 1, 1987, pp. 507-519.
[38]Culick, F. E. C., "Rotational Axisymmetric Mean Flow and Damping of Acoustic Waves in a Solid Propellant Rocket," *AIAA Journal,* Vol. 4, No. 8, 1966, pp. 1462-1464.
[39]Bragg, S. L., and Hawthorne, W. R., "Some Exact Solutions of the Flow through Annular Cascade Actuator Disks," *Journal of the Aeronautical Sciences,* Vol. 17, No. 4, 1950, pp. 243-249.
[40]Majdalani, J., "On Steady Rotational High Speed Flows: The Compressible Taylor-Culick Profile," *Proceedings of the Royal Society, London, Series A,* Vol. 463, No. 2077, 2007, pp. 131-162.